

# Quantifying Quasi-Fermi Level Splitting and Mapping its Heterogeneity in Atomically Thin Transition Metal Dichalcogenides

Mike Tebyetekerwa,\* Jian Zhang, Kun Liang, The Duong, Guru Prakash Neupane, Linglong Zhang, Boqing Liu, Thien N. Truong, Rabin Basnet, Xiaojing Qiao, Zongyou Yin, Yuerui Lu,\* Daniel Macdonald,\* and Hieu T. Nguyen\*

One of the most fundamental parameters of any photovoltaic material is its quasi-Fermi level splitting ( $\Delta\mu$ ) under illumination. This quantity represents the maximum open-circuit voltage ( $V_{oc}$ ) that a solar cell fabricated from that material can achieve. Herein, a contactless, nondestructive method to quantify this parameter for atomically thin 2D transition metal dichalcogenides (TMDs) is reported. The technique is applied to quantify the upper limits of  $V_{oc}$  that can possibly be achieved from monolayer  $WS_2$ ,  $MoS_2$ ,  $WSe_2$ , and  $MoSe_2$ -based solar cells, and they are compared with state-of-the-art perovskites. These results show that  $V_{oc}$  values of  $\approx 1.4$ ,  $\approx 1.12$ ,  $\approx 1.06$ , and  $\approx 0.93$  V can be potentially achieved from solar cells fabricated from  $WS_2$ ,  $MoS_2$ ,  $WSe_2$ , and  $MoSe_2$  monolayers at 1 Sun illumination, respectively. It is also observed that  $\Delta\mu$  is inhomogeneous across different regions of these monolayers. Moreover, it is attempted to engineer the observed  $\Delta\mu$  heterogeneity by electrically gating the TMD monolayers in a metal-oxide-semiconductor structure that effectively changes the doping level of the monolayers electrostatically and improves their  $\Delta\mu$  heterogeneity. The values of  $\Delta\mu$  determined from this work reveal the potential of atomically thin TMDs for high-voltage, ultralight, flexible, and eye-transparent future solar cells.


2D transition metal dichalcogenides (TMDs) have attracted significant research attention in the recent past.<sup>[1]</sup> This has been fueled by their novel and promising properties for future optoelectronics.<sup>[2,3]</sup> These properties include atomically thin flexibility and lightweight,<sup>[1,4]</sup> excellent optoelectronic properties courtesy of the quantum-confinement effects in their monolayers which improve their absorption efficiency,<sup>[5]</sup> and naturally occurring passivation of their surfaces making it possible to build various vertical heterostructures without lattice mismatch,<sup>[6]</sup> as is frequently encountered in conventional materials. Recently, 2D TMDs have demonstrated a strong potential to be used in future photovoltaic (PV) devices.<sup>[3]</sup> Numerous efforts have been performed by different research groups to demonstrate solar cells fabricated from 2D TMDs in various configurations such as vertical hetero van der Waals (vdW),<sup>[7]</sup> vertical doped homo p-n,<sup>[8]</sup> lateral hetero p-n,<sup>[9]</sup> lateral homo p-n,<sup>[10]</sup> local gate p-n,<sup>[11]</sup> and vertical<sup>[12]</sup> and lateral<sup>[13]</sup> Schottky structures. Overall, these devices have demonstrated power conversion efficiencies (PCEs) of up to a few percent in just a few nanometer-thick layers due to their strong light-matter interactions.<sup>[3,14]</sup> However, the TMD devices are yet to give reasonable performances, and to possess scalable technologies in comparison to the traditional PV technologies such as silicon (27.6%) and CdTe (22.1%) or even some other emerging technologies such as perovskite (23.7%) and quantum dot cells (16.6%).<sup>[15]</sup> Therefore, more insightful understanding of the fundamental properties of TMDs relevant to PV applications is significant for fabricating efficient devices.

Optical-based characterization is one of the most established and important class of techniques for investigating semiconductor materials' properties. This class of techniques has been employed widely on various large-scale (millimeters to meters) PV materials including silicon, perovskites and many others. For 2D TMDs whose surface areas are still at the micrometer scale, also numerous fundamental parameters such as the absorption coefficient,<sup>[16,17]</sup> refractive index ( $n$ ),<sup>[18]</sup> or exciton

M. Tebyetekerwa, Dr. J. Zhang, K. Liang, Dr. T. Duong, Dr. G. P. Neupane, Dr. L. Zhang, B. Liu, T. N. Truong, R. Basnet, Prof. Y. Lu, Prof. D. Macdonald, Dr. H. T. Nguyen  
Research School of Electrical  
Energy and Materials Engineering  
College of Engineering and Computer Science  
The Australian National University  
Canberra, ACT 2601, Australia  
E-mail: mike.tebyetekerwa@anu.edu.au; yuerui.lu@anu.edu.au;  
daniel.macdonald@anu.edu.au; hieu.nguyen@anu.edu.au

K. Liang, Prof. X. Qiao  
School of Mechatronic Engineering  
Beijing Institute of Technology  
Beijing 100081, China

Dr. Z. Yin  
Research School of Chemistry  
College of Chemistry  
The Australian National University  
Canberra, ACT 2601, Australia

 The ORCID identification number(s) for the author(s) of this article can be found under <https://doi.org/10.1002/adma.201900522>.

DOI: 10.1002/adma.201900522

binding energies<sup>[19]</sup> have been experimentally established using various optical-based techniques. However, no study of these materials has focused on quantifying their quasi-Fermi level splitting between electrons and holes ( $\Delta\mu$ ) under light illumination. From a thermodynamic standpoint, this quantity of a semiconductor material reflects the maximum open-circuit voltage ( $V_{oc}$ ) that a solar cell fabricated from that material can achieve.<sup>[20,21]</sup> It can be considered as an early indicator of the device performance at the material stage, and thus is critical for device modeling and optimization.

Herein, we report a contactless, nondestructive method to quantify and map spatial inhomogeneities of  $\Delta\mu$  in various commonly studied monolayer TMDs including WS<sub>2</sub>, MoS<sub>2</sub>, WSe<sub>2</sub>, and MoSe<sub>2</sub>. First, we explain the underlying principle of our technique. We then verify the crystalline nature of our materials using both micro-Raman and micro-photoluminescence ( $\mu$ -PL) spectroscopy. The results are then confirmed by atomic force microscopy (AFM) measurements. After that, we employ the technique to extract  $\Delta\mu$  from the monolayers of the four mechanically exfoliated TMDs mentioned above. We then continue mapping  $\Delta\mu$  for various areas on 2D TMDs to examine their inhomogeneities. After that, the results are compared with state-of-the-art quadruple-cation Cs<sub>0.07</sub>Rb<sub>0.03</sub>FA<sub>0.765</sub>MA<sub>0.135</sub>PbI<sub>2.55</sub>Br<sub>0.45</sub> perovskite films with thickness ranging from 260 to 460 nm based on which >20% efficiency solar cells (4 mm × 4 mm active area) have been demonstrated previously.<sup>[22]</sup> Finally, we present our preliminary results on engineering the observed  $\Delta\mu$  heterogeneity by electrically gating the TMD monolayers in a metal-oxide-semiconductor (MOS) configuration.

According to the generalized Planck law, the photon flux per energy interval  $dr_{em}(\hbar\omega)$ , emitted from a certain semiconductor under excitation into the entire hemisphere, is given by Equation (1)<sup>[20,21,23]</sup>

$$dr_{em}(\hbar\omega) = A(\hbar\omega) \times \frac{(\hbar\omega)^2}{4\pi^2\hbar^3c^2} \times \left[ \exp\left(\frac{\hbar\omega - \Delta\mu}{kT}\right) - 1 \right]^{-1} \quad (1)$$

where  $\hbar$  is the reduced Planck constant,  $k$  is Boltzmann's constant and  $c$  is the speed of light in the medium that the photons are emitted.  $A(\hbar\omega)$  is the absorbance of the emitting material and  $\Delta\mu$  is the chemical potential, i.e., the quasi-Fermi energy splitting, of electron-hole pairs under excitation. This relationship between the photon emission, absorbance, and chemical potential is applicable to any type of radiation including thermal and nonthermal emissions in both direct and indirect-gap semiconductors. In the case of thermal radiation, the quantity  $\Delta\mu$  simply becomes zero, and thus we have the traditional black-body thermal emission. A critical assumption in Equation (1) is that  $\Delta\mu$  is the same throughout the material thickness. If surface defects exist, the concentrations of holes and electrons can vary depthwise, leading to a change in this value.<sup>[20,24]</sup> As the TMDs investigated here have only one layer (1L) or two layers (2L), we assume that there is no variation across the material thickness. We also note that as long as  $\hbar\omega - \Delta\mu$  is at least three times  $kT$ , the constant “-1” in the expression  $\left[ \exp\left(\frac{\hbar\omega - \Delta\mu}{kT}\right) - 1 \right]$  can be neglected.

In photoluminescence (PL) experiments, spectra are captured in arbitrary units from a certain solid angle relative to the

sample surface. The detected photon flux ( $PL_{det}(\hbar\omega)$ ) contains only a fraction of the emitted photon flux ( $dr_{em}(\hbar\omega)$ ). Therefore, we can rewrite Equation (1) into new Equation (2)

$$\ln \left[ \frac{PL_{det}(\hbar\omega)}{SF \times C \times A(\hbar\omega) \times (\hbar\omega)^2} \right] = \frac{\Delta\mu}{kT} - \frac{\hbar\omega}{kT} \quad (2)$$

where SF is the scaling factor accounting for the detected fraction of the emitted photons and  $C$  is a physical constant  $1/(4\pi^2\hbar^3c^2)$ . From Equation (2), one can extract the quantity  $\Delta\mu$  from the detected PL spectrum  $PL_{det}(\hbar\omega)$  and absorbance spectrum  $A(\hbar\omega)$  of the material, if the scaling factor (SF) and sample temperature ( $T$ ) are known. The scaling factor can be determined by using a calibrated Lambertian spectralon, and various light sources with known intensities (see Note S1 in the Supporting Information for the calibration procedure). The absorbance spectrum of the TMDs can be obtained from the measured differential reflectance between the substrate and the sample (see the Experimental Section).<sup>[25]</sup> The actual sample temperature  $T$  under illumination can be extracted from the slope of the PL spectra.

TMD monolayers were first exfoliated on a gel substrate and then transferred to a cleaned quartz substrate (see Note S2 for substrate cleaning and Scheme S1 in the Supporting Information). Prior to transferring onto the quartz substrate, optical microscopy images were captured to identify the monolayers (Figure 1a). The optical contrast was used as a guide to distinguish the monolayers or bilayers of WS<sub>2</sub>, MoS<sub>2</sub>, WSe<sub>2</sub>, and MoSe<sub>2</sub> from the bulk material. To verify our expectations, AFM (Figure S2, Supporting Information), micro-PL (Figure 1b), and micro-Raman (Figure 1c) spectroscopy measurements were performed to confirm the number of exfoliated layers prior to further studies. The main PL peak positions in Figure 1b located at  $\approx 2.02$ , 1.89, 1.67, and 1.57 eV are emitted from the monolayers of WS<sub>2</sub>, MoS<sub>2</sub>, WSe<sub>2</sub>, and MoSe<sub>2</sub>, respectively. They match well with previous reports.<sup>[26,27]</sup> The Raman spectra acquired from 1L (Figure 1c), 2L and bulk TMDs (Figure S3, Supporting Information) are also provided. In MoSe<sub>2</sub> (Figure S3a, Supporting Information), the typical dominant Raman out-of-plane A<sub>1g</sub> mode of different layers can be observed (240.6, 241.7, and 243 cm<sup>-1</sup> for 1L, 2L, and bulk, respectively).<sup>[26,28]</sup> In MoS<sub>2</sub> (Figure S3b, Supporting Information), the separation between the in-plane E<sub>12g</sub> mode ( $\approx 385$  cm<sup>-1</sup> in 1L) and the out-of-plane A<sub>1g</sub> mode ( $\approx 404$  cm<sup>-1</sup> in 1L) increases with increasing thicknesses (1L < 2L < bulk), which is in agreement with previous reports.<sup>[26,29]</sup> In WS<sub>2</sub> (Figure S3c, Supporting Information), both expected A<sub>1g</sub> and E<sub>12g</sub> modes are observed at  $\approx 417$  and  $\approx 352$  cm<sup>-1</sup> for all thicknesses but the former's intensity increases with increasing thicknesses (1L < 2L < bulk).<sup>[30]</sup> In WSe<sub>2</sub> (Figure S3d, Supporting Information), a dominant peak is observed at  $\approx 250$  cm<sup>-1</sup> for 1L, 2L, and bulk material. This peak is much sharper for 1L and 2L than for the bulk. Another peak is observed at  $\approx 258$  cm<sup>-1</sup> for both 1L and 2L, but it is much clearer for 2L. Such observations have previously been ascribed to A<sub>1g</sub> mode (250 cm<sup>-1</sup>) and E<sub>12g</sub> mode degeneration (258 cm<sup>-1</sup>) in few-layer WSe<sub>2</sub> nanosheets.<sup>[31]</sup>

In Figure 2, we demonstrate the fitting details to extract  $\Delta\mu$  from the PL (in logarithmic scale) and absorbance spectra of the monolayer TMDs and perovskite materials. For

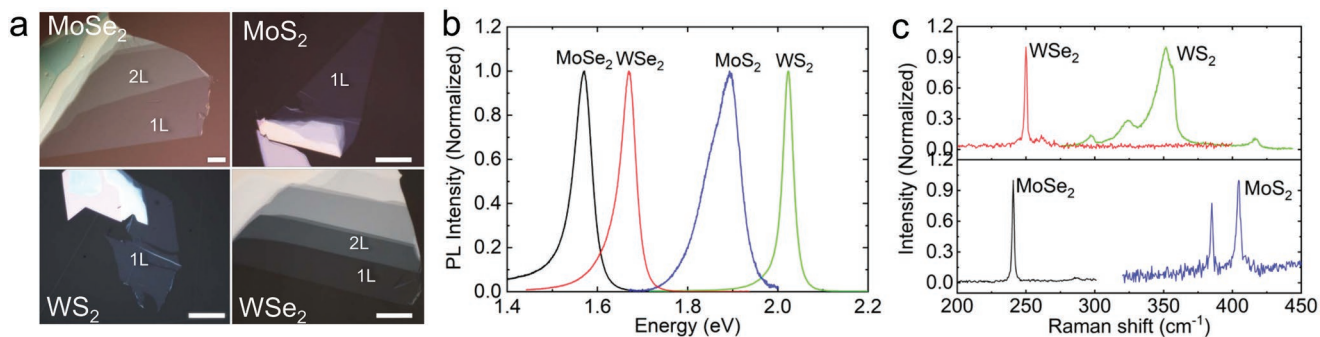


**Figure 1.** Transferred exfoliated monolayer TMDs on quartz substrates. a) Optical microscopy images (the scale bar is 20  $\mu\text{m}$ ), b) PL spectra, and c) Raman spectra of monolayer  $\text{WS}_2$ ,  $\text{MoS}_2$ ,  $\text{WSe}_2$ , and  $\text{MoSe}_2$ . The measurements were performed with an excitation wavelength of 532 nm at room temperature.

monolayer TMDs ( $\text{MoSe}_2$ ,  $\text{MoS}_2$ ,  $\text{WS}_2$ , and  $\text{WSe}_2$ ), two excitonic peaks (A and B) are known to be associated with interband transitions at the K point in the Brillouin zone.<sup>[16]</sup> They are separated due to the splitting of the valence band by spin-orbit coupling.<sup>[32]</sup> The energies of these two peaks on the absorbance

spectra must match those on the PL spectra. In Figure 2a–d, the A-excitonic peak is clearly revealed and matches between the PL and absorbance spectra. The B-excitonic PL peak is generally extremely weak and can only be observed with a much higher excitation power (e.g., see Figure S4 in the Supporting

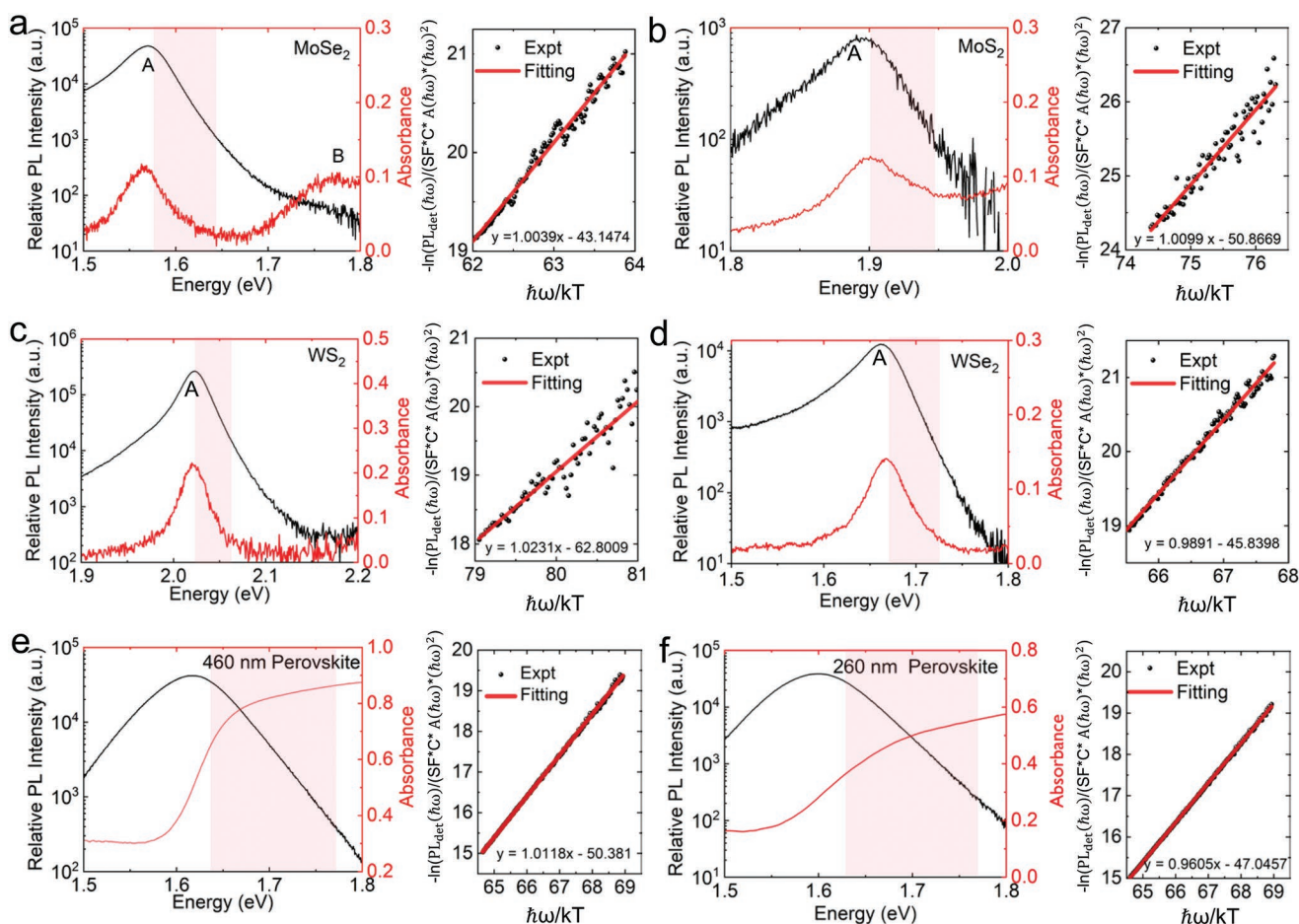


**Figure 2.** Room-temperature PL and absorbance spectra and fitting of the  $\ln\left[\frac{\text{PL}_{\text{det}}(\hbar\omega)}{\text{SF} \times \text{C} \times \text{A}(\hbar\omega) \times (\hbar\omega)^2}\right]$  term versus  $\hbar\omega/kT$ . a)  $\text{MoSe}_2$ , b)  $\text{MoS}_2$ , c)  $\text{WS}_2$ , d)  $\text{WSe}_2$ , e) 460 nm, and f) 260 nm quadruple-cation ( $\text{Cs}_{0.07}\text{Rb}_{0.03}\text{FA}_{0.765}\text{MA}_{0.135}\text{PbI}_{2.55}\text{Br}_{0.45}$ ) perovskite film (see scanning electron microscopy images in Figure S6 in the Supporting Information). The shaded areas highlight the fitted regions of interest. From the fitting results, the slopes approach unity, verifying consistency between the experiments and the theory outlined in Equation (2). “A” and “B” denote the A- and B-excitonic peaks.

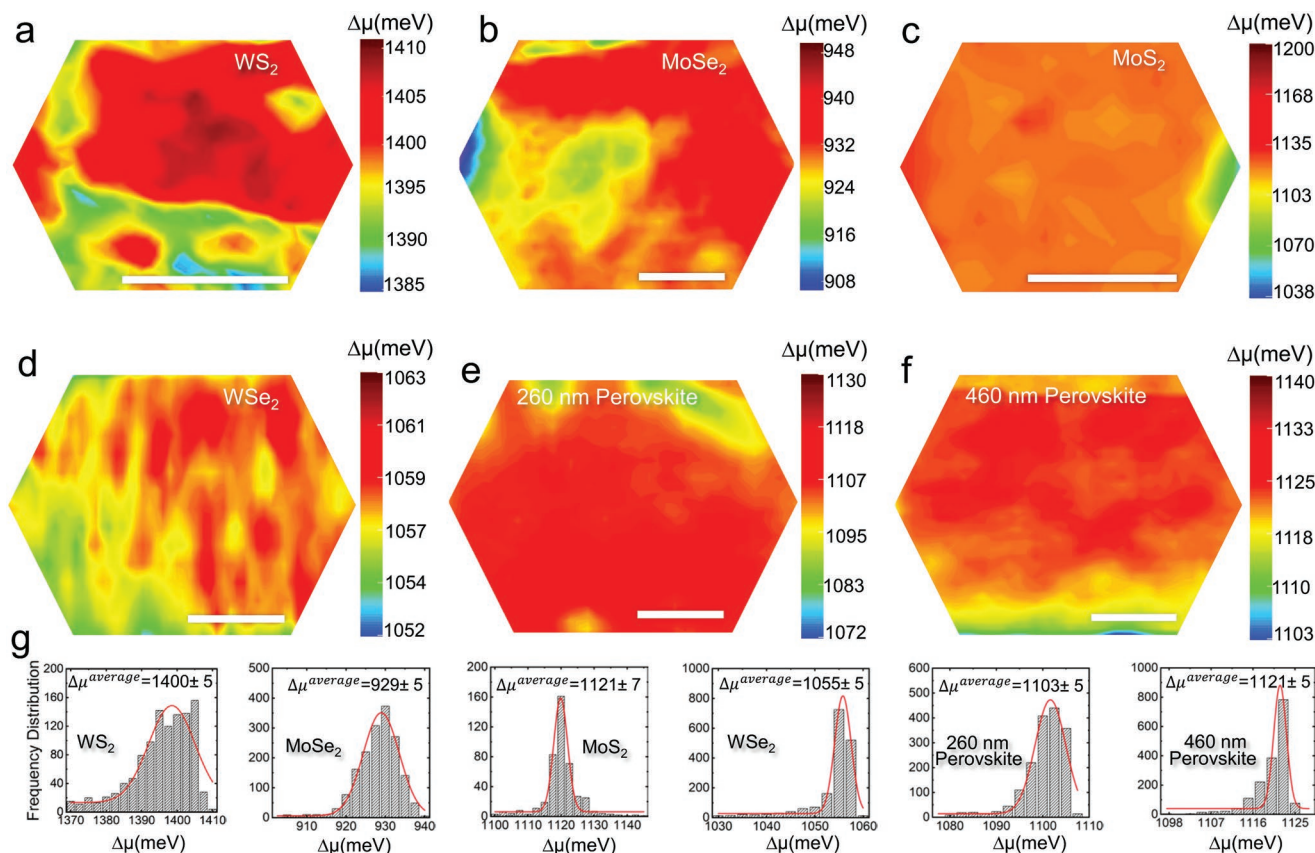


**Figure 3.**  $\Delta\mu$  mapping. a–f) Representative  $\Delta\mu$  maps of different monolayer TMDs (a–d) and perovskite materials (e–f). Inhomogeneities can be observed across various areas of all samples analyzed. g) Statistical distributions of  $\Delta\mu$  and their Gaussian fits of the investigated samples. The distributions were obtained from all the analyzed areas of the monolayers (see Figures S8–S11 in the Supporting Information), which had an area of at least  $200 \mu\text{m}^2$ . In (g), mean and standard deviation values of  $\Delta\mu$  are also given. The standard deviations were observed to vary between 5 and 7 meV depending on the area of interest. The scale bar is  $10 \mu\text{m}$ .

Information for  $\text{MoSe}_2$ ). This B-excitonic absorbance peak can be observed for  $\text{MoSe}_2$  (Figure 1b). For the other monolayer TMDs (Figure 2b–d), this peak is beyond the working ranges of our detector and laser source. In principle, either the A or B-excitonic peak could be used to extract  $\Delta\mu$  due to their similar origin. However, due to the weak PL intensity and out-of-range absorbance of the B-excitonic peak, we employ the A-excitonic peak to extract  $\Delta\mu$ . Also, the low-energy side of the A-exciton PL peak is reported to be often affected by defect luminescence.<sup>[33]</sup> Therefore, the high-energy sides of the A-exciton PL and absorbance spectra (shaded areas in Figure 2) are used to extract  $\Delta\mu$ . The monolayer absorbance spectra are obtained according to the details in Note S3 and Figure S5 in the Supporting Information. We noted no spatial heterogeneity of absorbance for the measured TMD monolayers (see Figure S5d in the Supporting Information). For comparison, PL and absorbance spectra from the perovskite films are also captured and displayed in Figure 2e,f and Figure S7 in the Supporting Information, for 260, 460, and 360 nm perovskite, respectively.

A direct way to verify our method is to plot the term  $\ln\left[\frac{\text{PL}_{\text{det}}(h\omega)}{\text{SF} \times C \times A(h\omega) \times (h\omega)^2}\right]$  in Equation (2) versus  $\hbar\omega/kT$ . If the experiments are consistent with the theory, the slope of  $\ln\left[\frac{\text{PL}_{\text{det}}(h\omega)}{\text{SF} \times C \times A(h\omega) \times (h\omega)^2}\right]$  versus  $\hbar\omega/kT$  must approach unity for

any semiconductor material according to Equation (2). The extracted slopes and their corresponding fittings are shown next to the PL and absorbance spectra for the monolayer TMDs (Figure 2a–d), the 460 nm (Figure 2e), 360 nm (Figure S7, Supporting Information), and 260 nm (Figure 2f) quadruple-cation perovskite film. From the slope, the sample temperature is also estimated to be  $298 \pm 5 \text{ K}$ . The uncertainty in the temperature ( $\pm 5 \text{ K}$ ) is obtained by fitting various samples, and this corresponds to  $\approx \pm 15 \text{ meV}$  uncertainty in the calculated  $\Delta\mu$ . As shown later, this value is much smaller than  $\Delta\mu$  variations among the monolayer TMDs and the perovskite. Also, the temperature is expected to be uniform for each sample within the small areas of mapping (tens of micrometers in both X and Y directions).

Now, we perform micro-PL spectroscopy ( $\mu$ -PLS) mapping to demonstrate the high value of this method to quantify the nonuniformity of the quasi-Fermi level splitting across various monolayer TMDs and the perovskite, as well as compare among them. The  $\mu$ -PLS maps provide an entire spectrum for every pixel in the X–Y map, allowing an extraction of the temperature and  $\Delta\mu$  with micrometer-scale spatial resolution. The resultant  $\Delta\mu$  maps are shown in Figure 3. Their corresponding PL/Raman intensity and peak energy maps are provided in Figures S8–S11 (TMDs), Figure S12 (PL maps), and Figure S13 ( $\Delta\mu$  maps) in the Supporting Information of quadruple-cation

perovskite. The values in Figure 3 have been all corrected for a 1 Sun intensity, which is relevant to evaluating performances of PV devices, by the formula  $\Delta\mu_{@1\text{Sun}} = \Delta\mu_{@636\text{Sun}} - (1/kT) \times \ln(636)$ . Here, 636 is the excitation intensity used in this work. This relation is commonly used to describe the relationship of  $V_{oc}$  under various illumination intensities, assuming that the diode ideality factor is equal to unity.<sup>[34]</sup> Also, the 1 Sun intensity is defined as an equivalent intensity of  $100\text{ mW cm}^{-2}$  from the 532 nm excitation source. Although this definition is different from the standard AM1.5G solar spectrum used for solar cell efficiency measurements, it provides a consistent way to compare among the samples and has been employed by numerous authors.<sup>[23,35,36]</sup> From Figure 3, one can observe that all the analyzed TMD monolayers (Figure 3a–d), together with the perovskites (Figure 3e–f), show spatial inhomogeneities of  $\Delta\mu$ . The locations with low values of  $\Delta\mu$  are obviously not desirable for PV applications as the maximum  $V_{oc}$  of finished solar cells at these locations would be capped by these low values. They, in turn, would affect the global device performance due to their interactions with adjacent locations. For perovskite materials, these inhomogeneities have been commonly observed and are attributed to local defects and/or material composition nonuniformity.<sup>[23,37]</sup> Herein, the observed inhomogeneity in TMDs can be attributed to the local defects within the monolayers. The observed inhomogeneity does not arise from the presence of multiple layers of TMDs, as our Raman maps confirm uniform individual layers (Figures S8–11c, Supporting Information).

From the measured areas, statistical spatial distributions of  $\Delta\mu$ , corresponding to maximum possible  $V_{oc}$  of solar cells at 1 Sun intensity if fabricated from the materials, are obtained (Figure 3g). The average values ( $\Delta\mu_{\text{average}}$ ) of  $\text{WS}_2$ ,  $\text{MoS}_2$ ,  $\text{WSe}_2$ , and  $\text{MoSe}_2$  are  $1400 \pm 5$ ,  $1121 \pm 7$ ,  $1055 \pm 5$ , and  $929 \pm 5$  meV, respectively. For the thin-layer quadruple-cation perovskite material, they are  $1103 \pm 5$  (260 nm),  $1111 \pm 5$  (360 nm) (Figure S13b, Supporting Information), and  $1121 \pm 5$  (460 nm). The noted results above, along with the PL peak energies, are summarized in Figure 4a. In principle, these extracted maximum  $V_{oc}$  ( $V_{oc,\text{max}} = \Delta\mu/e$  where  $e$  is electron unit charge) can be potentially achieved for solar cells fabricated from these

monolayer-based solar cells at 1 Sun illumination. To fortify this statement, we fabricate solar cells employing the 460 nm quadruple-cation perovskite film. With this perovskite film, we have consistently achieved over 20% PCE in a single-junction configuration<sup>[22]</sup> and over 26% PCE in a perovskite/Si tandem configuration.<sup>[38]</sup> The obtained  $V_{oc}$  of these highly efficient single-junction solar cells (PCE = 20.7%,  $4\text{ mm} \times 4\text{ mm}$  active area,  $V_{oc} = 1.172\text{ V}$ , short-circuit current =  $2.5\text{ mA cm}^{-2}$  and fill factor = 0.755) is similar to the  $\Delta\mu$  value extracted from the 460 nm quadruple-cation perovskite film ( $\approx 1.121\text{ eV}$ ) (see the cell structure and  $I$ – $V$  curves in Figure S14 in the Supporting Information).

It is worth noting that,  $\Delta\mu$  of the perovskite samples is found to be dependent on their thicknesses. In Figure 4a,  $\Delta\mu$  slightly decreases from 1121 to 1103 meV when the thickness reduces from 460 to 260 nm. On the other hand, despite the ultrathin nature of the TMD monolayers, their obtainable  $V_{oc}$  is still very high, which is much more than that of the matured silicon solar cell technology ( $744\text{ mV}$ <sup>[39]</sup> for the current world-record efficiency). The results demonstrate the high potential of this new class of materials for next generation PV devices. Here, although the method is demonstrated on 1L TMDs and perovskite materials, it can also be applied to other 2D semiconductor materials as well as 2L and few-layer TMDs. Indeed, we have demonstrated it on mechanically exfoliated 2L  $\text{MoSe}_2$  with  $\Delta\mu_{\text{average}}$  of  $818 \pm 5$  meV (Figure S15, Supporting Information). This value is much lower than that of the 1L  $\text{MoSe}_2$  ( $929 \pm 5$  meV) due to the lower emission efficiency of the 2L  $\text{MoSe}_2$ .

It should also be noted that, under illumination, after thermally relaxing down to stable energy states, the excited electron–hole pairs can either be extracted or recombine. The main PL peak position can be used to estimate the stable energy states where most of excess electrons and holes are distributed after the relaxation. However, even in ideal solar cells,  $V_{oc}$  is always lower than this peak energy value due to the thermodynamic detailed balance which requires equilibrium cells to reemit photons into the environment.<sup>[40]</sup> This is known as “Shockley–Queisser limit” of  $V_{oc}$  ( $V_{oc,S-Q}$ ). Therefore, a better comparison of  $\Delta\mu$  among the TMD materials should account

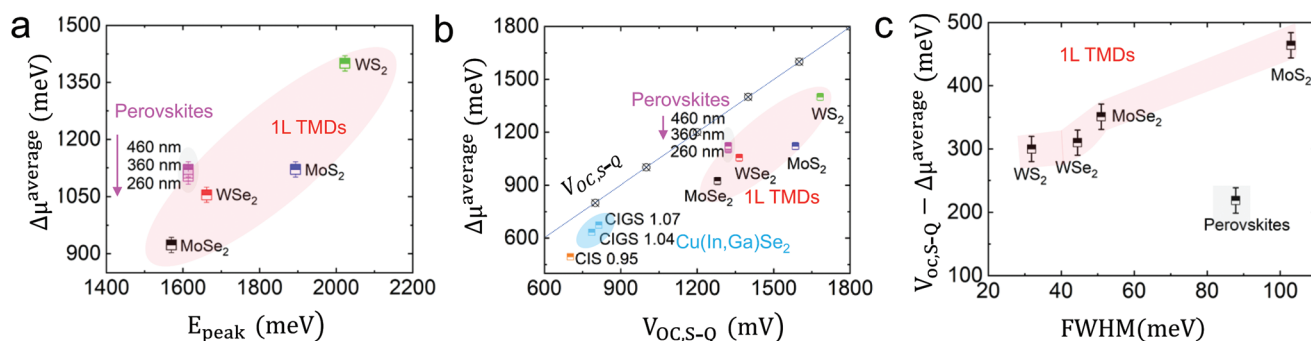


**Figure 4.** Performance comparison among various TMDs and other materials. a) Average experimental values of  $\Delta\mu_{\text{average}}$  versus PL peak energy ( $\Delta\mu_{\text{average}}$  vs  $E_{\text{peak}}$ ) of perovskites and monolayer TMDs. b)  $\Delta\mu_{\text{average}}$  versus “Shockley–Queisser limit” of  $V_{oc}$  ( $\Delta\mu_{\text{average}}$  vs  $V_{oc,S-Q}$ ) of thin-film perovskites,  $\text{Cu}(\text{In,Ga})\text{Se}_2$  (obtained from ref. [35]). [Note: CIS 0.95 is a thin-film semiconductor with a  $\text{Cu}:\text{In}$  ratio of 0.88 and a bandgap of 0.95 eV. CIS 1.04 and CIS 1.07 are  $\text{Cu}(\text{In,Ga})\text{Se}_2$  thin films with  $\text{Cu}:\text{InGa}$  ratios of 0.94 and 0.91, and bandgaps of 1.04 and 1.07 eV, respectively.] and monolayer TMDs. c) ( $V_{oc,S-Q} - \Delta\mu_{\text{average}}$ ) gap versus FWHM of the PL spectra of monolayer  $\text{WS}_2$ ,  $\text{MoS}_2$ ,  $\text{WSe}_2$ , and  $\text{MoSe}_2$  together with the thin-layer perovskite (average of 260, 360, and 460 nm). The error bar is  $\pm 20$  meV, consisting of the overall 5 meV standard deviation from mapping results and 15 meV from the temperature uncertainty.  $V_{oc,S-Q}$  values of the monolayer TMDs were estimated using their optical A-excitonic bandgap energies.

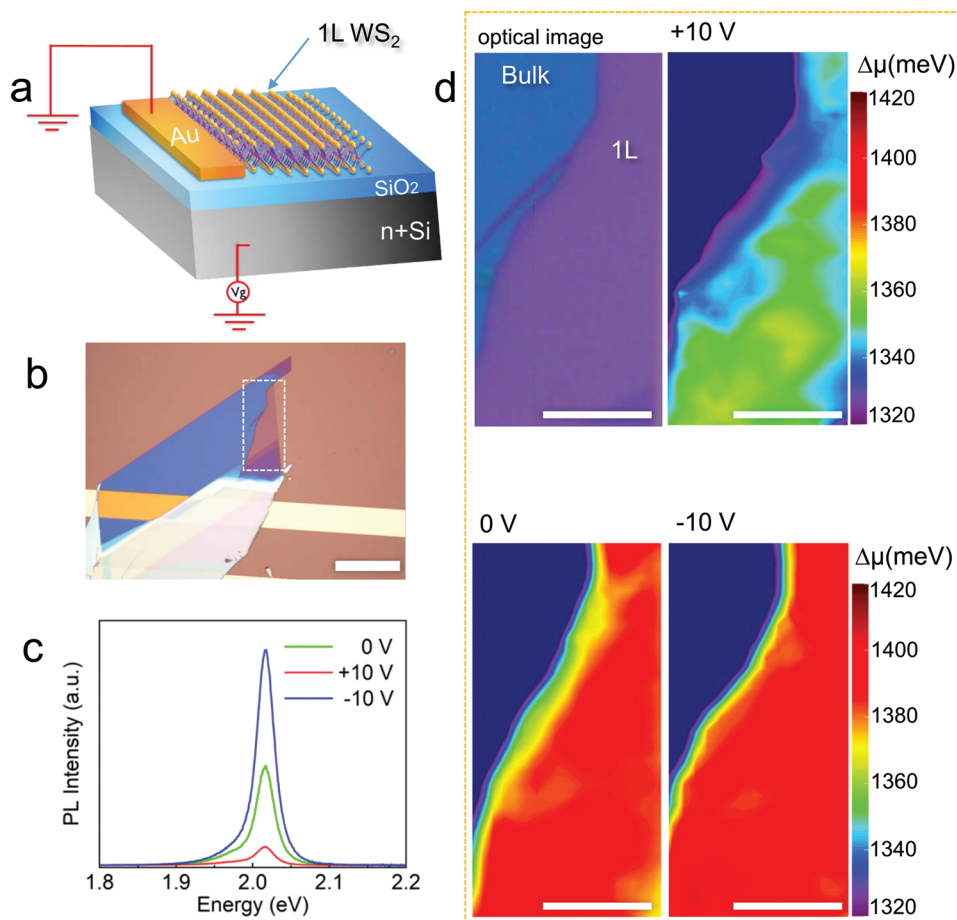


**Figure 5.** Effects of electrical gating on  $\Delta\mu$  of the monolayer  $\text{WS}_2$ . a) Schematic assembly of the monolayer-based MOS structure with electrical connections, b) optical microscopy image of the analyzed monolayer on the MOS setup (scale bar 50  $\mu\text{m}$ ), c) PL spectra obtained from the monolayer  $\text{WS}_2$  with back gate voltages of  $-10$ ,  $0$  and  $+10$  V and d) the corresponding mapping of  $\Delta\mu$  across the monolayer  $\text{WS}_2$  (scale bar 10  $\mu\text{m}$ ).

for this limit. In Figure 4b, we replot  $\Delta\mu_{\text{average}}$  versus  $V_{\text{oc,S-Q}}$ , along with reference data of a common thin film  $\text{Cu(In,Ga)Se}_2$  from the literature.<sup>[35]</sup> Also, in Figure 4c, we compare the  $V_{\text{oc,S-Q}} - \Delta\mu_{\text{average}}$  gap among the investigated materials. Smaller values mean closer to the fundamental Shockley–Queisser limit. The  $V_{\text{oc,S-Q}}$  value of each material is derived based on its PL peak energy position. From Figure 4c, the  $V_{\text{oc,S-Q}} - \Delta\mu_{\text{average}}$  gap of 1L  $\text{WS}_2$  is the smallest among the four TMDs. Moreover, this gap is found to increase with increasing full width at half-maximums (FWHMs) of the PL spectra from the TMDs (Figure 4c). As these 1L TMDs have direct bandgaps, the higher FWHM corresponds to the more disorder and defect states, leading to a bigger gap between  $\Delta\mu_{\text{average}}$  and  $V_{\text{oc,S-Q}}$ .

From the experimental analysis, the 1L  $\text{WS}_2$  shows the highest  $\Delta\mu$  value of  $\approx 1400$  meV, the smallest  $V_{\text{oc,S-Q}} - \Delta\mu$  gap of  $\approx 280$  meV, and the sharpest luminescence spectrum. This coupled with other previously observed properties in 1L  $\text{WS}_2$  such as its exceptional emission quantum yield and improved spin-orbit coupling,<sup>[41]</sup> and capabilities to demonstrate nonblinking photon emission<sup>[42]</sup> could make 1L  $\text{WS}_2$  to be a more promising candidate for optoelectronic applications than the other three TMDs. Therefore, we also attempt to engineer  $\Delta\mu$  of 1L  $\text{WS}_2$  with an electrostatic doping technique by electrically gating the

$\text{WS}_2$  monolayer in a metal-oxide-semiconductor configuration (Figure 5a,b). 1L  $\text{WS}_2$  is known to act as an n-type semiconductor.<sup>[43]</sup> Figure 5c shows that its PL intensity, and thus  $\Delta\mu$ , is improved significantly with less electron doping (i.e., lower back-gate voltage,  $10 \text{ V} < 0 \text{ V} < -10 \text{ V}$ ), consistent with previous reports.<sup>[43]</sup> Moreover, in Figure 5d,  $\Delta\mu$  homogeneity across the entire sample is clearly improved with less electron doping. This could be due to the fact that the initial doping level of the TMD monolayer is sensitive to the defect levels and the initial variation might be large, thus causing the observed  $\Delta\mu$  heterogeneity. However, with a lower back-gate voltage (i.e., less electron doping), the doping becomes more uniform, leading to the improved uniformity of  $\Delta\mu$ . These preliminary results demonstrate that indeed both  $\Delta\mu$  and its homogeneity can be manipulated by the doping levels inside 1L TMDs. This finding opens a promising avenue for defect engineering in the 1L TMDs for PV applications.

In summary, we have reported a contactless, nondestructive method to quantify the quasi-Fermi level splitting in atomically thin TMD monolayers using the generalized Planck law. The obtained quasi-Fermi splitting values, which are considered as the maximum obtainable open-circuit voltages of atomically thin TMD-based photovoltaic devices, are found to vary

across the areas of the investigated samples. These findings demonstrate that the monolayer TMD materials still need to be improved for photovoltaic applications as the layer nonuniformity can detrimentally affect their device performance. However, despite this fact, some of these atomically thin layers have been found to potentially yield a very high overall open-circuit voltage beyond even the high-performance perovskite films. This property is promising for future PV technologies. In addition, we have validated our technique with quadruple-cation perovskite films and confirmed that the extracted quasi-Fermi level splitting matches well with the open-circuit voltage obtained from highly efficient perovskite solar cells. Finally, we have presented some initial results on engineering the value and homogeneity of this parameter by manipulating the doping level inside the monolayers.

## Experimental Section

**TMD Monolayer Preparation:** From the bulk of crystals of individual TMDs, monolayers (1L) of various TMDs were mechanically exfoliated, using a scotch tape method, onto a clean gel substrate (Gel-Pak). After that, the obtained layers were transferred from the gel film to a cleaned quartz substrate prior to measurements.

**Perovskite Preparation:** Quadruple-cation perovskite ( $\text{Cs}_{0.07}\text{Rb}_{0.03}\text{FA}_{0.765}\text{MA}_{0.135}\text{PbI}_{2.55}\text{Br}_{0.45}$ ) films with thickness of 260–460 nm were employed. See Note S4 in the Supporting Information for their detailed preparation.

**Photoluminescence and Raman Characterization:** Micro-photoluminescence and micro-Raman spectroscopy were performed using a Horiba LabRAM system equipped with a confocal microscope a charge-coupled device (CCD) Si detector (detection range between 400 and 1000 nm), and a 50 $\times$  objective lens (numerical aperture = 0.55). The excitation source was a continuous-wave 532 nm diode-pumped solid-state (DPSS) laser. The laser light was focused onto the sample surface with a diameter of  $\approx 1 \mu\text{m}$ . The on-sample excitation power was  $\approx 0.5 \mu\text{W}$ , corresponding to a power density of  $\approx 636 \text{ Sun}$ . The spectral response of the entire system was determined with a calibrated tungsten–halogen light source. The photoluminescence spectra were all corrected for the spectral response of the system.

**Absorbance Measurements:** The absorbance of the thin-layer perovskite film was obtained using a PerkinElmer 1050 spectrometer with an integrating sphere detector. The absorbance spectrum  $A(\hbar\omega) = 1 - R(\hbar\omega) - T(\hbar\omega)$  was determined from reflectance ( $R(\hbar\omega)$ ) and transmittance ( $T(\hbar\omega)$ ) measurements of the sample in the wavelength range from 450 to 1000 nm. The absorbance of the 1L/2L TMDs was determined from the differential reflectance between the sample on substrate and the substrate. The reflectance of the sample on substrate and the substrate was measured using the same  $\mu\text{-PL/Raman}$  system with a broad band radiation from a supercontinuum NKT laser whose tunable wavelength range is 480–2000 nm. The measured differential reflectance from the substrate and the sample was then used to obtain the absorbance ( $A(\hbar\omega)$ ) of the material using the formula described in Note S3 in the Supporting Information.<sup>[44]</sup>

## Supporting Information

Supporting Information is available from the Wiley Online Library or from the author.

## Acknowledgements

This work was supported by the Australian Renewable Energy Agency (ARENA) through Research Grant RND017. The authors acknowledge

the facilities and technical support from the Australian National Fabrication Facility (ANFF), ACT Node, and the Australian Microscopy & Microanalysis Research Facility at the Centre of Advanced Microscopy and at the Australian National University. M.T. acknowledges the research support of the Australian Government Research Training Program (RTP) Scholarship. H.T.N. acknowledges the fellowship support from the Australian Centre for Advanced Photovoltaics (ACAP). K.L. and X.J.Q. acknowledge the support from the International Graduate Exchange Program of the Beijing Institute of Technology. H.T.N. conceived the idea, designed the overall experiments, and supervised the project. D.M. and Y.L. consulted the scientific direction and cosupervised the project. M.T. fabricated samples and performed all measurements. H.T.N. performed simulations. J.Z., K.L., G.P.N., L.Z, B.L., T.N.T., R.B., X.Q., and Z.Y. contributed to the 2D material fabrication and experimental setup. T.D. fabricated and characterized quadruple-cation perovskite films and solar cells. M.T. and H.T.N. analyzed the data and wrote the manuscript. All authors contributed to the discussion of the results and reviewed the manuscript.

## Conflict of Interest

The authors declare no conflict of interest.

## Keywords

2D materials, open-circuit voltage, photoluminescence, photovoltaic cells, quasi-Fermi level splitting, transition metal dichalcogenides

Received: January 22, 2019

Revised: March 16, 2019

Published online:

- [1] Q. H. Wang, K. Kalantar-Zadeh, A. Kis, J. N. Coleman, M. S. Strano, *Nat. Nanotechnol.* **2012**, *7*, 699.
- [2] X. Duan, C. Wang, A. Pan, R. Yu, X. Duan, *Chem. Soc. Rev.* **2015**, *44*, 8859.
- [3] L. Wang, L. Huang, W. C. Tan, X. Feng, L. Chen, X. Huang, K.-W. Ang, *Small Methods* **2018**, *2*, 1700294.
- [4] F. Xia, H. Wang, D. Xiao, M. Dubey, A. Ramasubramaniam, *Nat. Photonics* **2014**, *8*, 899.
- [5] L. Britnell, R. M. Ribeiro, A. Eckmann, R. Jalil, B. D. Belle, A. Mishchenko, Y. J. Kim, R. V. Gorbachev, T. Georgiou, S. V. Morozov, A. N. Grigorenko, A. K. Geim, C. Casiraghi, A. H. C. Neto, K. S. Novoselov, *Science* **2013**, *340*, 1311.
- [6] a) A. K. Geim, I. V. Grigorieva, *Nature* **2013**, *499*, 419; b) K. Novoselov, A. Mishchenko, A. Carvalho, A. C. Neto, *Science* **2016**, *353*, aac9439.
- [7] a) C.-H. Lee, G.-H. Lee, A. M. Van Der Zande, W. Chen, Y. Li, M. Han, X. Cui, G. Arefe, C. Nuckolls, T. F. Heinz, *Nat. Nanotechnol.* **2014**, *9*, 676; b) R. Cheng, D. Li, H. Zhou, C. Wang, A. Yin, S. Jiang, Y. Liu, Y. Chen, Y. Huang, X. Duan, *Nano Lett.* **2014**, *14*, 5590; c) M. M. Furchi, A. Pospischil, F. Libisch, J. Burgdörfer, T. Mueller, *Nano Lett.* **2014**, *14*, 4785; d) A. Pezeshki, S. H. H. Shokouh, T. Nazari, K. Oh, S. Im, *Adv. Mater.* **2016**, *28*, 3216; e) N. Flöry, A. Jain, P. Bharadwaj, M. Parzefall, T. Taniguchi, K. Watanabe, L. Novotny, *Appl. Phys. Lett.* **2015**, *107*, 123106; f) M. M. Furchi, A. A. Zechmeister, F. Hoeller, S. Wachter, A. Pospischil, T. Mueller, *IEEE J. Sel. Top. Quantum Electron.* **2017**, *23*, 106.
- [8] a) Y. Jin, D. H. Keum, S. J. An, J. Kim, H. S. Lee, Y. H. Lee, *Adv. Mater.* **2015**, *27*, 5534; b) S. Wi, H. Kim, M. Chen, H. Nam,

- L. J. Guo, E. Meyhofer, X. Liang, *ACS Nano* **2014**, *8*, 5270; c) H.-M. Li, D. Lee, D. Qu, X. Liu, J. Ryu, A. Seabaugh, W. J. Yoo, *Nat. Commun.* **2015**, *6*, 6564.
- [9] a) X. Duan, C. Wang, J. C. Shaw, R. Cheng, Y. Chen, H. Li, X. Wu, Y. Tang, Q. Zhang, A. Pan, *Nat. Nanotechnol.* **2014**, *9*, 1024; b) M.-Y. Li, Y. Shi, C.-C. Cheng, L.-S. Lu, Y.-C. Lin, H.-L. Tang, M.-L. Tsai, C.-W. Chu, K.-H. Wei, J.-H. He, *Science* **2015**, *349*, 524.
- [10] M. S. Choi, D. Qu, D. Lee, X. Liu, K. Watanabe, T. Taniguchi, W. J. Yoo, *ACS Nano* **2014**, *8*, 9332.
- [11] a) B. W. Baugher, H. O. Churchill, Y. Yang, P. Jarillo-Herrero, *Nat. Nanotechnol.* **2014**, *9*, 262; b) A. Pospischil, M. M. Furchi, T. Mueller, *Nat. Nanotechnol.* **2014**, *9*, 257; c) D. J. Groenendijk, M. Buscema, G. A. Steele, S. Michaelis de Vasconcellos, R. Bratschitsch, H. S. van der Zant, A. Castellanos-Gomez, *Nano Lett.* **2014**, *14*, 5846.
- [12] M. Shanmugam, C. A. Durcan, B. Yu, *Nanoscale* **2012**, *4*, 7399.
- [13] M. Fontana, T. Deppe, A. K. Boyd, M. Rinzan, A. Y. Liu, M. Paranjape, P. Barbara, *Sci. Rep.* **2013**, *3*, 1634.
- [14] X. Yu, K. Sivula, *ACS Energy Lett.* **2016**, *1*, 315.
- [15] Best Research-Cell Efficiencies, National Renewable Energy Laboratory, <https://www.nrel.gov/pv/assets/pdfs/best-research-cell-efficiencies.pdf> (accessed: March 2019).
- [16] a) H. L. Liu, C. C. Shen, S. H. Su, C. L. Hsu, M. Y. Li, L. J. Li, *Appl. Phys. Lett.* **2014**, *105*, 201905; b) J. A. Wilson, A. Yoffe, *Adv. Phys.* **1969**, *18*, 193.
- [17] C. Ho, Y. Huang, K. Tiong, P. Liao, *Phys. Rev. B* **1998**, *58*, 16130.
- [18] a) G. Wang, S. Zhang, X. Zhang, L. Zhang, Y. Cheng, D. Fox, H. Zhang, J. N. Coleman, W. J. Blau, J. Wang, *Photonics Res.* **2015**, *3*, A51; b) Y. V. Morozov, M. Kuno, *Appl. Phys. Lett.* **2015**, *107*, 083103.
- [19] a) M. M. Ugeda, A. J. Bradley, S.-F. Shi, H. Felipe, Y. Zhang, D. Y. Qiu, W. Ruan, S.-K. Mo, Z. Hussain, Z.-X. Shen, *Nat. Mater.* **2014**, *13*, 1091; b) A. Hanbicki, M. Currie, G. Kioseoglou, A. Friedman, B. Jonker, *Solid State Commun.* **2015**, *203*, 16.
- [20] P. Wurfel, *J. Phys. C: Solid State Phys.* **1982**, *15*, 3967.
- [21] a) K. Schick, E. Daub, S. Finkbeiner, P. Würfel, *Appl. Phys. A: Solids Surf.* **1992**, *54*, 109; b) E. Daub, P. Würfel, *Phys. Rev. Lett.* **1995**, *74*, 1020.
- [22] a) J. Peng, T. Duong, X. Zhou, H. Shen, Y. Wu, H. K. Mulmudi, Y. Wan, D. Zhong, J. Li, T. Tsuzuki, *Adv. Energy Mater.* **2017**, *7*, 1601768; b) J. Peng, Y. Wu, W. Ye, D. A. Jacobs, H. Shen, X. Fu, Y. Wan, T. Duong, N. Wu, C. Barugkin, H. T. Nguyen, D. Zhong, J. Li, T. Lu, Y. Liu, M. N. Lockrey, K. J. Weber, K. R. Catchpole, T. P. White, *Energy Environ. Sci.* **2017**, *10*, 1792.
- [23] G. El-Hajje, C. Momblona, L. Gil-Escrig, J. Ávila, T. Guillemot, J.-F. Guillemoles, M. Sessolo, H. J. Bolink, L. Lombez, *Energy Environ. Sci.* **2016**, *9*, 2286.
- [24] G. Lasher, F. Stern, *Phys. Rev.* **1964**, *133*, A553.
- [25] a) R. Frisenda, Y. Niu, P. Gant, A. J. Molina-Mendoza, R. Schmidt, R. Bratschitsch, J. Liu, L. Fu, D. Dumcenco, A. Kis, *J. Phys. D: Appl. Phys.* **2017**, *50*, 074002; b) W. Zhao, Z. Ghorannevis, L. Chu, M. Toh, C. Kloc, P.-H. Tan, G. Eda, *ACS Nano* **2012**, *7*, 791.
- [26] P. Tonndorf, R. Schmidt, P. Böttger, X. Zhang, J. Börner, A. Liebig, M. Albrecht, C. Kloc, O. Gordan, D. R. Zahn, *Opt. Express* **2013**, *21*, 4908.
- [27] a) P. Rivera, J. R. Schaibley, A. M. Jones, J. S. Ross, S. Wu, G. Aivazian, P. Klement, K. Seyler, G. Clark, N. J. Ghimire, J. Yan, D. G. Mandrus, W. Yao, X. Xu, *Nat. Commun.* **2015**, *6*, 6242; b) A. Huang, E. Ray, K. Seyler, P. Rivera, E. Wong, P. Nyugen, G. Clark, X. Xu, *Bull. Am. Phys. Soc.* **2016**, *61*; c) K. F. Mak, C. Lee, J. Hone, J. Shan, T. F. Heinz, *Phys. Rev. Lett.* **2010**, *105*, 136805.
- [28] S.-Y. Chen, C. Zheng, M. S. Fuhrer, J. Yan, *Nano Lett.* **2015**, *15*, 2526.
- [29] a) A. Molina-Sanchez, L. Wirtz, *Phys. Rev. B* **2011**, *84*, 155413; b) C. Lee, H. Yan, L. E. Brus, T. F. Heinz, J. Hone, S. Ryu, *ACS Nano* **2010**, *4*, 2695.
- [30] A. Berkdemir, H. R. Gutiérrez, A. R. Botello-Méndez, N. Perea-López, A. L. Elías, C.-I. Chia, B. Wang, V. H. Crespi, F. López-Urías, J.-C. Charlier, H. Terrones, M. Terrones, *Sci. Rep.* **2013**, *3*, 1755.
- [31] H. Zeng, G.-B. Liu, J. Dai, Y. Yan, B. Zhu, R. He, L. Xie, S. Xu, X. Chen, W. Yao, *Sci. Rep.* **2013**, *3*, 1608.
- [32] Z. Zhu, Y. Cheng, U. Schwingenschlögl, *Phys. Rev. B* **2011**, *84*, 153402.
- [33] J. W. Christopher, B. B. Goldberg, A. K. Swan, *Sci. Rep.* **2017**, *7*, 14062;
- [34] a) S. R. Wenham, M. A. Green, M. E. Watt, R. Corkish, A. Sproul, *Applied Photovoltaics*, Routledge, London **2013**; b) T. Markvart, K. Bogus, *Solar Electricity*, Vol. 6, John Wiley & Sons, New York **2000**.
- [35] H. Elanzeery, F. Babbe, M. Melchiorre, F. Werner, S. Siebentritt, *Prog. Photovoltaics* **2018**, *26*, 437.
- [36] I. L. Braly, D. W. deQuilettes, L. M. Pazos-Outón, S. Burke, M. E. Ziffer, D. S. Ginger, H. W. Hillhouse, *Nat. Photonics* **2018**, *12*, 355.
- [37] a) K. H. Ahn, T. F. Seman, T. Lookman, A. Bishop, *Phys. Rev. B* **2013**, *88*, 144415; b) Q. Sun, P. Fassel, Y. Vaynzof, *ACS Appl. Energy Mater.* **2018**, *1*, 2410.
- [38] T. Duong, Y. Wu, H. Shen, J. Peng, X. Fu, D. Jacobs, E.-C. Wang, T. C. Kho, K. C. Fong, M. Stocks, E. Franklin, A. Blakers, N. Zin, K. McIntosh, W. Li, Y.-B. Cheng, T. P. White, K. Weber, K. Catchpole, *Adv. Energy Mater.* **2017**, *7*, 1700228.
- [39] K. Yoshikawa, H. Kawasaki, W. Yoshida, T. Irie, K. Konishi, K. Nakano, T. Uto, D. Adachi, M. Kanematsu, H. Uzu, K. Yamamoto, *Nat. Energy* **2017**, *2*, 17032.
- [40] W. Shockley, H. J. Queisser, *J. Appl. Phys.* **1961**, *32*, 510.
- [41] L. Yuan, L. Huang, *Nanoscale* **2015**, *7*, 7402.
- [42] N. Peimyoo, J. Shang, C. Cong, X. Shen, X. Wu, E. K. Yeow, T. Yu, *ACS Nano* **2013**, *7*, 10985.
- [43] J. Shang, X. Shen, C. Cong, N. Peimyoo, B. Cao, M. Eginligil, T. Yu, *ACS Nano* **2015**, *9*, 647.
- [44] a) E. Hecht, *Optics*, 4th ed., Addison-Wesley Longman Inc, Reading, MA **1998**; b) K. He, C. Poole, K. F. Mak, J. Shan, *Nano Lett.* **2013**, *13*, 2931.